

Preparation of high-performance Cu_2Se thermoelectric materials by the KCl flux method and research on thermoelectric transport performance

Yonggui Tao(陶永贵), Chisheng Deng(邓池升), Jicheng Li(李吉成), Wen Ge(葛文), Ying Zhang(张盈), Yujie Xiang(向玉婕), and Shukang Deng(邓书康)

Citatio: Chin. Phys. B, 2025, 34 (**9**): 097306. DOI: 10.1088/1674-1056/add4fa
http://cpb.iphy.ac.cn; http://iopscience.iop.org/cpb

What follows is a list of articles you may be interested in

In-plane negative magnetoresistance and quantum oscillations in van der Waals antiferromagnet $DyTe_3$

Qi Qi(齐琦), Senhao Lv(吕森浩), Ke Zhu(祝轲), Yaofeng Xie(谢耀锋), Guojing Hu(胡国静), Zhen Zhao(赵振), Guoyu Xian(冼国裕), Yechao Han(韩烨超), Yang Yang(杨洋), Lihong Bao(鲍丽宏), Xiao Lin(林晓), Hui Guo(郭辉), Haitao Yang(杨海涛), and Hong-Jun Gao(高鸿钧)

Chin. Phys. B, 2025, 34 (**7**): 077305. DOI: 10.1088/1674-1056/adcc87

Enhanced thermoelectric properties of the topological phase of monolayer HfC

Wenlai Mu(母文来), Nisar Muhammad(穆罕默德·尼萨), Baojuan Dong(董宝娟), Nguyen Tuan Hung(阮俊兴), Huaihong Guo(郭怀红), Riichiro Saito(斋藤理一郎), Weijiang Gong(公卫江), Teng Yang(杨腾), and Zhidong Zhang(张志东)

Chin. Phys. B, 2025, 34 (**5**): 057301. DOI: 10.1088/1674-1056/adbd17

$GaInX_3$ (X = S, Se, Te): Ultra-low thermal conductivity and excellent thermoelectric performance

Zhi-Fu Duan(段志福), Chang-Hao Ding(丁长浩), Zhong-Ke Ding(丁中科), Wei-Hua Xiao(肖威华), Fang Xie(谢芳), Nan-Nan Luo(罗南南), Jiang Zeng(曾犟), Li-Ming Tang(唐黎明), and Ke-Qiu Chen(陈克求)

Chin. Phys. B, 2024, 33 (**8**): 087302. DOI: 10.1088/1674-1056/ad47e3

Enhanced thermoelectric properties in two-dimensional monolayer Si_2BN by adsorbing halogen atoms

Cheng-Wei Wu(吴成伟), Changqing Xiang(向长青), Hengyu Yang(杨恒玉), Wu-Xing Zhou(周五星), Guofeng Xie(谢国锋), Baoli Ou(欧宝立), and Dan Wu(伍丹)

Chin. Phys. B, 2021, 30 (**3**): 037304. DOI: 10.1088/1674-1056/abd163

Thermoelectric effects and topological insulators

Yong Xu(徐勇)

Chin. Phys. B, 2016, 25 (**11**): 117309. DOI: 10.1088/1674-1056/25/11/117309

Preparation of high-performance Cu_2Se thermoelectric materials by the KCl flux method and research on thermoelectric transport performance

Yonggui Tao(陶永贵)[1], Chisheng Deng(邓池升)[1], Jicheng Li(李吉成)[1,2], Wen Ge(葛文)[1], Ying Zhang(张盈)[1], Yujie Xiang(向玉婕)[1], and Shukang Deng(邓书康)[1,†]

[1] *School of Energy and Environmental Science, Yunnan Normal University, Kunming* 650500, *China*

[2] *School of Intelligent Science and Engineering, Yunnan Technology and Business University, Kunming* 650201, *China*

(Received 25 February 2025; revised manuscript received 30 April 2025; accepted manuscript online 7 May 2025)

This study achieves a notable enhancement in the thermoelectric performance of copper selenide compounds exhibiting liquid-like characteristics via an innovative processing method. A KCl flux-assisted high-temperature melting and slow-cooling strategy was employed to fabricate nanolayered Cu_2Se $(KCl)_x$ materials ($x = 0$–3, denoted as S_0–S_3). Systematic characterization reveals that the coexistence of α and β phases at room temperature creates favorable conditions for optimizing carrier transport. XPS analysis confirms the substitution of low-binding-energy Se^{2-} by high-binding-energy Cl^- ions within the lattice, effectively suppressing copper ion migration and remarkably improving the material's structural stability. Microstructural investigations demonstrate that all samples exhibit nanolayered stacking architectures abundant with edge dislocations. This multiscale defect architecture induces strong phonon scattering effects. Hall measurements indicate that the KCl flux-assisted processing facilitates the formation of highly ordered nanostructures, thereby enhancing carrier mobility and structural stability. Although the carrier concentration exhibits a slight decrease compared with the flux-free samples, the significant improvement in microstructural quality plays a crucial role in the synergistic optimization of electrical conductivity and the Seebeck coefficient. Notably, sample S_2 exhibited a considerable electrical conductivity, reaching approximately 1.0×10^5 $S{\cdot}m^{-1}$ at 300 K. More strikingly, the cooperative effect of high-density edge dislocations and dopant atoms elevates material entropy, enabling sample S_3 to attain an ultralow lattice thermal conductivity of 0.55 $W{\cdot}m^{-1}{\cdot}K^{-1}$ at 350 K. Through multi-mechanism coordination, sample S_2 achieved a high ZT value of 1.45 at 700 K, representing a 2.7-fold improvement compared with traditional synthesis methods. This work provides new insights into performance optimization of liquid-like thermoelectric materials through defect engineering and entropy manipulation.

Keywords: thermoelectric effects, low thermal conductivity, liquid-like, flux method

PACS: 73.50.Lw, 74.25.fc, 65.20.–w, 06.60.Ei

DOI: 10.1088/1674-1056/add4fa **CSTR:** 32038.14.CPB.add4fa

1. Introduction

In the context of the global energy crisis, the emergence of thermoelectric technology, driven by the Seebeck and Peltier effects, provides a promising avenue for sustainable energy solutions. It plays a crucial role in waste heat recovery, cooling technologies and the transformation of energy systems.[1,2] Thermoelectric materials are particularly effective in collecting and reutilizing waste heat.[3,4] In recent years, thermoelectric technology has gained widespread application in electronic devices and space technologies, due to its advantages such as silent operation and the absence of moving components. However, despite these benefits, its energy conversion efficiency remains relatively low compared with that of other energy harvesting methods. This challenge has driven the global research community to prioritize the development of advanced thermoelectric materials with enhanced performance. The dimensionless thermoelectric figure of merit (ZT) is a widely employed metric for assessing the efficiency of thermoelectric materials.[5] It is expressed as $ZT = S^2\sigma\kappa$, where S represents the Seebeck coefficient, σ denotes electrical conductivity and κ signifies the total thermal conductivity. As indicated by this relation, thermoelectric materials with superior performance necessitate high σ, a large S and low κ. Nevertheless, these parameters are interrelated, making it challenging to enhance material performance by modifying any single parameter in isolation, which constitutes a major bottleneck in the current advancement of thermoelectric materials.[6] In recent years, advanced decoupling techniques, including nanoengineering, band structure optimization, interface engineering and entropy manipulation, have significantly improved both the performance and stability of thermoelectric materials.

Cu_2Se is a prototypical 'electron crystal-phonon glass' thermoelectric material, characterized by high electrical conductivity and relatively low thermal conductivity. This makes it a promising candidate for thermoelectric power generation in medium- to high-temperature applications.[7] Cu_2Se is a phase-change ionic thermoelectric material that exists as a

†Corresponding author. E-mail: skdeng@126.com

© 2025 Chinese Physical Society and IOP Publishing Ltd. All rights, including for text and data mining, AI training, and similar technologies, are reserved.

stable α-phase below 414 K and transforms to the β-phase, known as the anti-fluorite structure, above 414 K. Within the reversible $\alpha \rightarrow \beta$ phase transition range, critical phonon scattering occurs,[8] significantly reducing the thermopower and enabling ZT to reach 2.3 at 400 K. β-phase Cu_2Se exhibits a space group of $Fm\bar{3}m$, wherein Se^{2-} ions form a rigid face-centered cubic lattice framework, with each ion occupying a vertex of the cubic unit cell. The Cu^+ ions exhibit a predominantly random distribution within the interstitial sites of the cubic lattice, although a notable localization occurs at the 8(c) and 32(f) Wyckoff positions. Owing to the disordered distribution of Cu^+ ions, high ionic mobility is achieved,[9] effectively suppressing the material's thermal conductivity. Simultaneously, the rigid face-centered cubic sublattice of Se^{2-} ions provides a stable electron transport network, thereby conferring superior electronic properties. Cu_2Se has been synthesized using various techniques, such as chemical synthesis,[10] spark plasma sintering (SPS),[11] hydrothermal methods, ball milling, hot pressing and combinations thereof. For instance, Zhao *et al.*[12] synthesized Cu_2Se using a hydrothermal method followed by hot pressing, thereby creating Cu_2Se/MXene composite bulk materials with a ZT_{max} of 1.77 at 923 K. Similarly, Tang *et al.*[13] employed a rapid, self-propagating, high-temperature synthesis method to fabricate BiCuSeO–Cu_2Se composites integrated with graphene interfaces, which improved the crystal structure, significantly reduced the thermal conductivity and ultimately yielded a peak ZT of 2.82 at 1000 K. Moreover, Yin *et al.*[14] utilized spark plasma sintering (SPS) to promote the quasi-homogenization of ternary elements, successfully synthesizing Ge-doped Cu_2Se with an average ZT of 0.56 over the temperature range 323–723 K. Wang *et al.*[15] prepared nitrogen-doped Cu_2Se via a chemical method and applied it to sodium and potassium ion batteries, demonstrating a promising integration of thermoelectric and electrochemical functionalities. Although these methods have enabled the achievement of high ZT values, they are often associated with complex procedures, high fabrication costs and material defects, which collectively undermine the thermal stability of the resulting materials.

Flux-assisted methods are recognized for their environmental friendliness and cost-effectiveness. By enabling crystal growth at temperatures below the melting point of the target material, these approaches help maintain a dynamic equilibrium of elemental composition during the growth process, resulting in more uniform elemental distributions and high-quality crystals. Commonly used flux materials include NaCl,[16] KCl[17] and Na_2CO_3.[18] In our previous work,[19] Cu_2Se crystals synthesized with NaCl flux achieved a peak ZT of 1.57 at 700 K. However, variations in atomic viscosity among different flux materials can substantially influence the crystal quality and thermoelectric transport properties of the final samples. In this study, we employed KCl, a flux material with a lower melting point, to ensure the formation of a more homogeneous melt at high temperatures. This approach optimized the liquation–precipitation process and promoted uniform crystal growth. By combining the flux method with high-temperature melting and slow cooling, high-performance Cu_2Se thermoelectric materials were successfully fabricated. Furthermore, we systematically investigated the chemical composition, microcrystalline structure and correlation with thermoelectric transport properties.

2. Experiment

2.1. Material preparation

Cu_2Se crystals were fabricated through KCl flux-assisted melting combined with a precisely controlled slow-cooling technique. The process utilized high-purity Cu (99.99%), Se (99.99%) and KCl (99.99%) granules. These were mixed in stoichiometric ratios corresponding to Cu_2Se $(KCl)_x$ ($x = 0$, 1, 2, 3) and labeled as S_0, S_1, S_2 and S_3, respectively. The raw materials were precisely weighed using a high-accuracy balance and sealed under vacuum in quartz tubes with carbon-coated inner walls. The sealed tubes were placed in a box furnace and heated at a rate of 3 K·min^{-1} from 300 K to 1443 K. The mixture was held at this temperature for 12 h to ensure complete melting and homogenization. The temperature was then reduced to 1273 K over 2 h, and subsequently cooled slowly to 773 K over 120 h. Finally, the samples were permitted to gradually return to room temperature within the furnace. To isolate the crystals from any remaining flux, KCl was dissolved in deionized water, resulting in the recovery of high-purity Cu_2Se crystals.

2.2. Material characterization

The phase composition of all samples was analyzed using x-ray diffraction (XRD; Ultima IV, Cu K_α, $\lambda = 1.5403$ Å). The cross-sectional morphology and elemental distribution were examined using a field emission scanning electron microscope (SEM; FEI Inspect F50) equipped with an energy dispersive x-ray spectrometer (EDX; Oxford Inca X-act). The crystal plane spacing, dislocations and defects within the crystal structure were studied using transmission electron microscopy (TEM; Tecnai G20) and selected area electron diffraction (SAED). Hall coefficients at 300 K were measured using a Hall effect tester (HL5500) under a magnetic field strength of 0.5 T. The Seebeck coefficient of the material was measured in the temperature range 300–500 K under vacuum conditions, using copper–nickel alloy (Cu55%) as a reference material. In the same temperature range, electrical conductivity was measured by the four-probe method with a stable

current source of 20 mA. Thermal diffusivity within the same temperature range was determined using the laser flash method (LFA 457, Netzsch) under an inert gas flow.

2.3. Error analysis

In this study, all measurements were conducted on three independently synthesized samples for each composition. The data are reported as mean values with standard deviations. Statistical analysis and curve fitting were performed using OriginPro 2024 (OriginLab Corporation), employing one-way analysis of variance at a 95% confidence level, followed by Tukey's post hoc test ($p < 0.05$) for multiple comparisons. Error bars indicate the standard deviations derived from the triplicate measurements. Experimental errors primarily originate from variations in sample preparation, contact resistance instability and instrument resolution limitations. The relative standard deviation (RSD) for all datasets was maintained below 5%, confirming the high reproducibility and reliability of the thermoelectric measurements.

3. Results and discussion

3.1. Characterization of the phase structure in the samples

Figure 1(a) shows the XRD test results for Cu_2Se $(KCl)_x$ ($x = 0$, 1, 2, 3) samples prepared using the KCl flux method. Table 1 lists the lattice parameters corresponding to the different phase structures of all the samples. As the initial content of KCl flux (x) increased, the lattice constants gradually decreased. The main diffraction peaks of all samples at 300 K can be assigned to α-Cu_2Se (PDF #47-1448) and partial β-Cu_2Se (PDF #76-0136), indicating the coexistence of α- and β-phases at room temperature, consistent with a previous report.[20] Figure 1(b) shows the enlarged XRD peaks corresponding to the (250), (410) and (211) planes of α-Cu_2Se for all samples. The Bragg diffraction peaks of the samples synthesized using the KCl flux method progressively shifted to higher angles, suggesting a reduction in the lattice parameters with increasing KCl content. Table 1 summarizes the variation of lattice constants and densities, determined by the Archimedes method, as a function of the KCl stoichiometric ratio. The gradual incorporation of KCl leads to a reduction in the lattice constants, likely due to the substitution of Se^{2-} ions by smaller-radius Cl^- ions in the lattice.[21] With an increase in the KCl flux stoichiometric ratio, the characteristic peaks of the (211) and (111) planes are significantly enhanced, whereas the intensity of the (410) peak is gradually diminished. This phenomenon can be attributed to the KCl flux promoting the preferential growth along the (211) and (111) planes in Cu_2Se, resulting in the corresponding enhancement of their diffraction peaks. Furthermore, in situ XRD measurements were conducted on the Cu_2Se $(KCl)_x$ ($x = 2$) sample. The results reveal that, as the temperature increases, Cu_2Se exhibits a distinct phase transition behavior, corroborated by previous research.[22] At room temperature, the stable α-phase is the dominant phase in Cu_2Se. However, the XRD patterns revealed the presence of weak signals corresponding to the characteristic peaks of the β-phase, indicating the coexistence of both α- and β-phases. As further temperature increases, the diffraction peaks increasingly overlap with the characteristic peaks of the β-phase, suggesting the completion of the $\alpha \rightarrow \beta$ phase transition.

To clarify the valence states of the elements in Cu_2Se $(KCl)_x$ samples, x-ray photoelectron spectroscopy (XPS) was performed on all samples. As shown in Fig. 2(a), the Cu 2p spectra exhibit two main peaks located at approximately 932.5 eV (Cu $2p_{3/2}$) and 952.2 eV (Cu $2p_{1/2}$), with a

Table 1. Lattice parameters and densities of all samples.

Samples Cu_2Se $(KCl)_x$ ($x = 0,1,2,3$)	Phase structure	a	b	c	V (Å^3)	ρ (g·cm^{-3})
S_0	Monoclinic	14.027	20.330	3.969	1130.84	6.80
S_1	Monoclinic	13.833	20.393	3.932	1109.32	6.74
	Cubic	5.842	5.843	5.843	199.45	
S_2	Monoclinic	13.781	20.420	3.914	1101.34	6.65
	Cubic	5.838	5.838	5.838	198.98	
S_3	Monoclinic	13.928	20.293	3.878	1096.17	6.52
	Cubic	5.807	5.807	5.807	195.81	

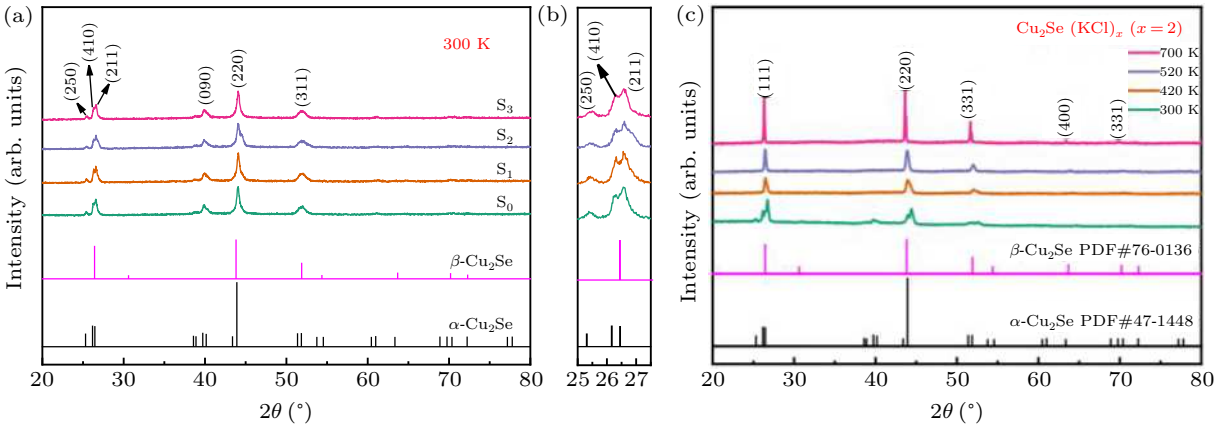


Fig. 1. (a) XRD full spectra. (b) Magnified local diffraction peaks of the samples. (c) *In situ* XRD of the Cu_2Se $(KCl)_2$ sample.

spin–orbit splitting of about 19.9 eV, indicating the presence of monovalent copper (Cu^+).[23] With increase in the stoichiometric ratio of the KCl flux, the Cu 2p binding energy gradually shifts toward higher values. This shift is likely due to the doping effect of Cl^- ions. Specifically, Cl^- has a significantly higher electronegativity than Se^{2-}. When Cl^- partially substitutes for Se^{2-} in the lattice, the resulting Cu–Cl bonds are more polar than Cu–Se bonds. This change redistributes the valence band electron cloud[24,25] and reduces the local electron density around Cu^+. As a result, the decreased electron density weakens the electronic shielding of Cu^+, enhances the effective nuclear attraction on valence electrons and facilitates the enhancement of binding energy. In addition, TEM analysis reveals a high density of dislocation defects in samples prepared via the KCl flux method. This phenomenon is closely related to the auxiliary doping of K^+ ions. K^+ incorporation introduces local lattice stress, which further modulates the electronic environment of Cu^+. The combined effects ultimately result in a systematic shift of the Cu 2p binding energy toward higher values.

The XPS spectra of Se 3d are shown in Fig. 2(b). The spin–orbit splitting is approximately 0.86 eV, which agrees well with the standard splitting for selenium. This confirms that selenium exists in the -2 oxidation state within the Cu_2Se matrix.[26,27] As the proportion of KCl flux rises, the Se 3d binding energy first decreases and then returns to its initial value. This non-monotonic trend may be attributed to flux-assisted crystal growth. The presence of KCl promotes better crystallinity, which reduces local lattice distortion and defect state density at Se sites. As a result, the chemical environment of Se^{2-} becomes less constrained by local lattice stress. The reduced internal stress lowers the confinement of valence electrons, leading to a slight decrease in Se 3d binding energy.[28] At higher KCl concentrations, Cl^- ions partially substitute Se^{2-} in the lattice. The formation of Cu–Cl bonds alters the original coordination structure of selenium. Simultaneously, K^+ ions, due to their relatively large ionic radius, tend to occupy interstitial positions within the lattice. This leads to local charge imbalance, slight lattice distortion and defect reconstruction.[29] These combined effects introduce greater structural complexity and chemical instability around Se atoms, ultimately resulting in a slight increase in the Se 3d binding energy.

Figures 2(c) and 2(d) present the high-resolution XPS spectra of Cl 2p and K 2p for samples prepared using the KCl flux method. The Cl 2p peaks appear at 198.04 eV and 200.14 eV, corresponding to the -1 oxidation state of chlorine.[30] At lower x values, Cl^- ions primarily substitute into the lattice and form highly polar Cl–Cu bonds. In this configuration, Cl experiences a stronger local electric field, resulting in a higher binding energy. As the KCl content increases, Cl^- doping approaches saturation. The high local concentration of Cl^- ions leads to charge crowding and enhanced electrostatic repulsion, which slightly weakens the effective binding environment. Consequently, the Cl 2p binding energy exhibits a slight downward shift.[31]

The K 2p core-level spectrum exhibits two peaks at 294.78 eV and 292.98 eV, with a spin–orbit splitting of approximately 2.77 eV. This value aligns well with that of standard potassium,[32] indicating that K atoms are present in the $+1$ oxidation state within the Cu_2Se lattice framework. With increasing flux content, K^+ ions are progressively distributed within lattice interstices and interfacial regions, and tend to accumulate at grain boundaries and defect sites. In these areas, K^+ may interact electrostatically with exposed Se^{2-} termination sites, forming weak coordination structures. This enhances the local crystal field around K atoms and results in a slight upward shift in the K 2p binding energy.[33]

The XPS results collectively confirm the successful incorporation of Cl and K into the Cu_2Se lattice. These dopants are expected to significantly influence the thermoelectric transport properties of the material.

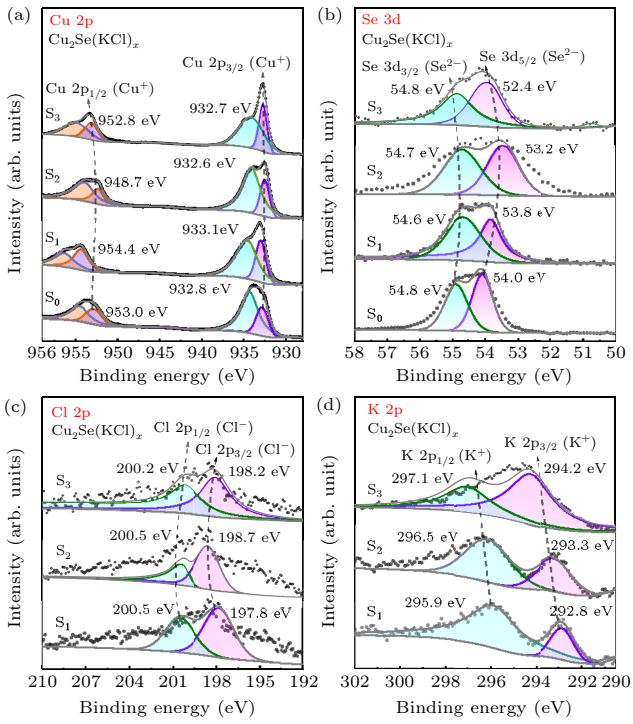


Fig. 2. XPS spectra of all samples: (a) Cu 2p, (b) Se 3d, (c) Cl 2p, (d) K 2p.

3.2. SEM and TEM analysis of the samples

As shown in Fig. 3(a1), the cross-sectional SEM image of the Cu_2Se $(KCl)_x$ ($x = 2$) reveals a nanolayered structure with layer thicknesses ranging from $\sim$ 110 nm to $\sim$ 165 nm. The dense interfaces formed between adjacent nanolayers act as prominent phonon scattering sites, effectively disrupting the coherent propagation of heat-carrying phonons throughout the material. As the phonon mean free path in Cu_2Se typically

ranges from tens to hundreds of nanometers, the nanoscale periodicity introduced by the layered architecture effectively matches this scale, leading to frequent phonon–interface interactions. These additional scattering events substantially reduce the phonon relaxation time, thereby impeding the transport of thermal energy and resulting in a marked decrease in lattice thermal conductivity.[34–36] No significant macroscopic defects were observed in the material, indicating that Cu_2Se synthesized using the KCl flux possesses a well-formed layered structure and high density. Figures 3(a2)–3(a6) show the EDS analysis of the samples prepared using the KCl flux method. The elements are uniformly distributed across the material, suggesting that the synthesized samples possess consistent composition and exceptional crystallinity. In addition, trace amounts of Cl and K are observed in the material. Figures 3(b)–3(e) show the stacked nanolayered structures for samples with $x = 0$, 1, 2 and 3, with layer thicknesses ranging from $\sim$ 110 nm to $\sim$ 165 nm. To further investigate the distribution of elements within the material, EDS testing was conducted on sample S_2. As illustrated in Fig. 3(g), the EDS spectrum for $x = 2$ reveals an approximate Cu:Se ratio of 2:1, thereby validating the synthesis of a high-quality Cu_2Se sample, which is in accordance with previously reported data.[37] The spectrum also shows that Cl and K are evenly distributed in small amounts, which further confirms that the KCl not only serves as a flux but also participates in the formation of the Cu_2Se lattice. As shown in Fig. 3(h), with an increase in the stoichiometric ratio of the KCl flux, the sample exhibits more interfaces, which are beneficial for optimizing its thermoelectric performance.

To further investigate the material's microstructural characteristics, including its crystal structure, crystallographic indices and internal defects and dislocations, we performed TEM characterization on all samples synthesized using the KCl flux method.

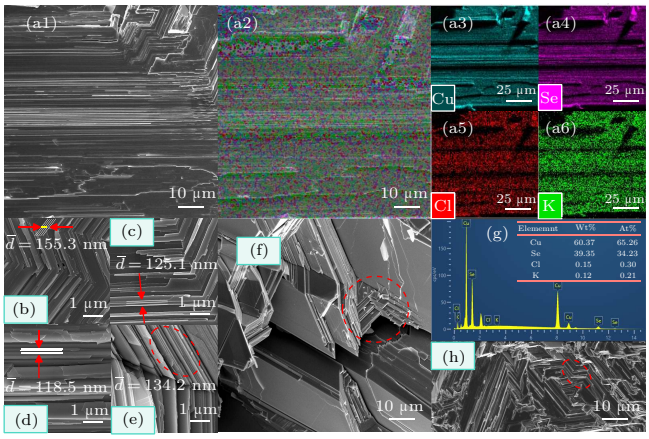


Fig. 3. (a1)–(a6) FESEM images of sample S_2 and elemental mapping analysis of Cu, Se, Cl and K. (b)–(e) Nanolayer structure images of samples S_0–S_3. (f) Cross-sectional morphology of a Cu_2Se $(KCl)_2$ sample. (g) Elemental distribution spectrum of sample S_2. (h) Cross-sectional morphology of S_3.

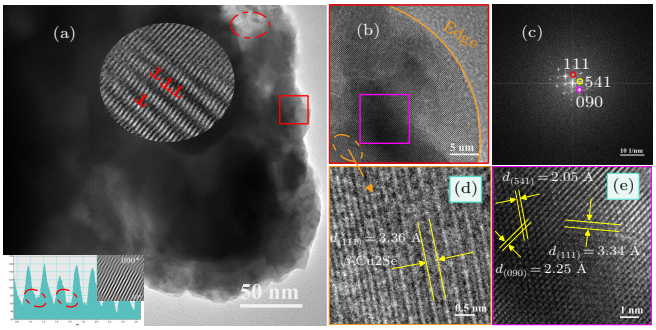


Fig. 4. (a) High-resolution TEM image of sample S_2 at 300 K. (b) Magnified image of the selected area in sample S_2. (c) SAED pattern of the square region. (d) Magnified image of the elliptical region indicated by the arrow. (e) Interplanar spacings between different crystal facets.

Figure 4(a) presents a high-resolution transmission electron microscopy (HRTEM) image of sample S_2, highlighting its overall high crystallinity. In the magnified elliptical region, a high density of edge dislocations is observed, which further reduces the κ of the material by promoting enhanced scattering of heat-carrying phonons.[38] The lower-left panel of Fig. 4(a) presents the lattice fringe profile extracted from the HRTEM image of the Cu_2Se sample. The observed fringes correspond to the (090) crystal planes with an interplanar spacing of approximately 2.26 Å. The presence of irregular intervals between major peaks and fine secondary peaks indicates a high density of dislocations and local lattice distortions within the material.[39] This feature further confirms that, despite the existence of well-ordered (090) planes, a significant number of crystallographic defects are simultaneously present in the sample. Figure 4(b) provides an enlarged view of the square region in panel (a), in which clear lattice fringes are visible, indicating Cu_2Se grains with different crystallographic orientations. The SAED pattern of the square region in panel (b) shows clearly visible diffraction spots, as presented in panel (c). The interplanar spacings for the α-phase (111), (541) and (090) crystal planes are measured to be 3.34 Å, 2.05 Å and 2.25 Å, respectively, are consistent with the XRD results. This finding confirms that the KCl flux effectively promotes the orderly growth of crystals during synthesis. Figure 4(d) shows a TEM image of sample S_2, presenting a local magnified view of the elliptical region (marked by an arrow) in panel (b). The uniform lattice arrangement indicates the presence of high-quality Cu_2Se grains. Fast Fourier transform (FFT) and inverse fast Fourier transform (IFFT) analyses of the selected area revealed a lattice spacing of 3.36 Å, confirming the existence of the β-phase.[40] This result demonstrates that the KCl flux effectively suppresses phase transition during the synthesis, enabling a small fraction of Cu_2Se to remain in the β-phase at room temperature, which contributes to improving the structural stability of Cu_2Se. The high-resolution TEM image shown in Fig. 4(e) reveals a dense crystal structure with significantly improved lattice ordering, indicating that KCl, acting

as a flux, substantially improves crystal quality during the material synthesis process.

3.3. Thermoelectric transport properties of Cu_2Se $(KCl)_x$ (x = 0, 1, 2, 3) samples

As evidenced by the results in Table 2, the carrier concentration (n) of Cu_2Se samples synthesized via the flux method (samples S_1 and S_2) is significantly lower than that of the directly melted sample S_0, exhibiting an order-of-magnitude variation. Although the carrier mobility (μ_H) shows a slight upward trend, its overall variation remains nearly constant. These results are further corroborated by Fig. S2(a), which presents the dependence of n and μ_H on the KCl stoichiometric ratio. The decrease in carrier concentration primarily arises from the microstructural modifications induced during flux-assisted synthesis. As previously discussed, the formation of uniform nanolayered architectures and the introduction of a high density of dislocations and defects, evidenced by SEM and TEM analyses, act as potential carrier trapping centers, thereby reducing the effective free carrier density. Notably, sample S_2 exhibits a certain degree of recovery in carrier concentration compared with S_1, reaching 1.18×10^{20} cm^{-3}, which approaches the optimal carrier concentration range for achieving high thermoelectric performance.[41] This improvement is attributed to the moderate substitution of Se^{2-} by Cl^- ions promoted by an appropriate amount of KCl flux, leading to the formation of shallow acceptor states that enhance hole concentration,[42] as confirmed by the uniform elemental distribution observed in EDS mappings. Furthermore, the formation of dangling bonds at original Cu ion sites facilitates the migration of electrons from adjacent sites to these unsaturated bonds, further contributing to the increase in hole concentration. Importantly, during this process, the carrier mobility remains almost unaffected,[43] indicating that the structural quality is well preserved. The temperature dependence of n and μ_H for sample S_2 is depicted in Fig. S2(b). With increasing temperature from 300 K to 700 K, the carrier concentration progressively increases, consistent with thermally activated carrier excitation behavior typically observed in narrow-bandgap semiconductors such as Cu_2Se. The elevated thermal energy promotes carrier excitation from intrinsic defect levels and facilitates the delocalization of carriers from localized states near dislocations and interfaces, leading to an increase in effective carrier density.

Table 2. All samples' carrier concentration and mobility.

Samples Cu_2Se $(KCl)_x$	Hall coefficient ($cm^3 \cdot C^{-1}$)	n (10^{20} cm^{-3})	μ_H ($cm^2 \cdot V^{-1} \cdot s^{-1}$)
S_0	0.0208	3.00	43.28
S_1	0.0800	0.78	44.98
S_2	0.0528	1.18	45.17
S_3	0.1178	0.53	48.16

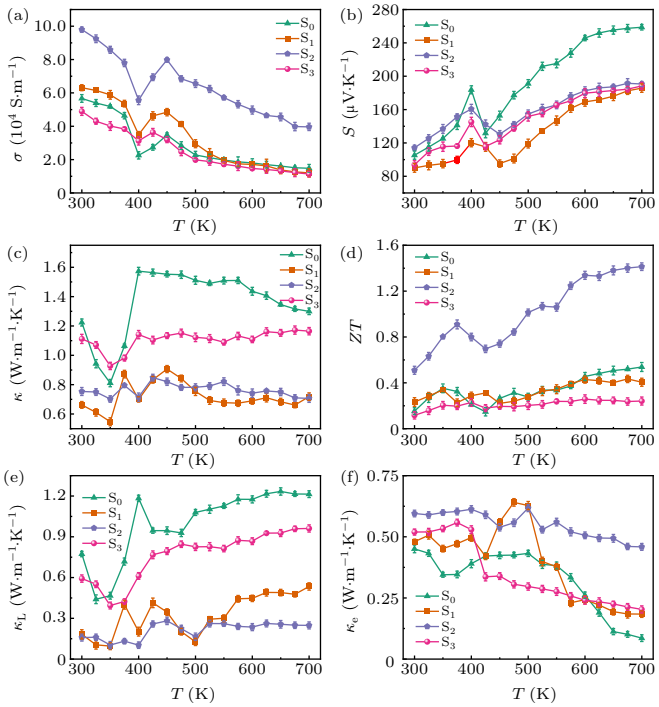


Fig. 5. (a) Electrical conductivity of all samples. (b) Seebeck coefficient. (c) Total thermal conductivity. (d) ZT value. (e) Lattice thermal conductivity. (f) Carrier thermal conductivity.

Meanwhile, the carrier mobility monotonically decreases with temperature, mainly due to enhanced phonon scattering and intensified carrier–interface scattering associated with the defect-rich layered microstructures.

Figure 5 illustrates the temperature-dependent thermoelectric transport characteristics of all samples. According to the data presented in Fig. 5(a), the electrical conductivity (σ) of each sample exhibited a decline as the temperature was raised from 300 K to 700 K. demonstrating the typical behavior of degenerative semiconductors. The amplitude of fluctuation of conductivity for sample S_3 in the vicinity of the phase-transition temperature was observed to diminish significantly. This phenomenon may be attributed to the increase in the content of the β-phase at room temperature as the quantity of KCl flux rises. This result is in agreement with the previous microscopic structural and phase analyses. Owing to the elevated n, the σ of sample S_3 attains a value of $\sigma = 9.8 \times 10^4$ S·m^{-1} at 300 K. Moreover, the electrical conductivity of sample S_3 decreases continuously across the entire temperature range, consistent with the trend in Table 2 where both n and μ_H decrease. This behavior is probably due to the increase in the KCl stoichiometric ratio within the overall system, resulting in a greater substitution of Cu^+ ions by K^+ ions. However, as the binding energy of the outermost electron of K is lower than that of Cu (as illustrated in Fig. 2), the dangling bonds near K^+ ions possess a weaker electron-trapping ability. Consequently, the carrier concentration in sample S_3 is reduced. The positive Seebeck coefficients observed for all the samples confirm that they exhibit p-type semiconductor behavior. At approx-

imately 410 K, a sharp change in the Seebeck coefficient (S) occurs due to the phase transition from α to β, which is consistent with the literature report.[44] As discussed earlier, due to the dual-phase structure around 300 K in the samples prepared with KCl, the fluctuation in S around 410 K is less pronounced compared with that of the directly melted sample S_0. Among all the samples, S_2 shows the highest S in the high-temperature region, reaching $S_{max} = 190\ \mu V{\cdot}K^{-1}$ at 700 K. According to the single parabolic band model, S is given by the following expression:[45]

$$S = m^* \frac{8\pi^2 k_B^2}{3e\hbar^2}\left(\frac{\pi}{3n}\right)^{\frac{2}{3}} T, \tag{1}$$

where m^* is the effective mass, k_B is the Boltzmann constant, T is the absolute temperature, e is the electron charge, $\hbar$ represents the reduced Planck's constant and n is the carrier concentration. This equation evidently demonstrates that the S of the material is positively correlated with the n, while being directly proportional to the effective mass. In addition to being related to the band structure, m^* of the material is significantly influenced by the carrier concentration. It is expressed as $m^* = ne\tau$, where τ is the average relaxation time of the carriers. If the influence of the band structure on m^* is neglected, the higher the n, the larger the S. This explains why S of sample S_2 is higher than that of the other flux-grown samples in this study.

Figure 5(c) depicts the relationship between the total thermal conductivity (κ) and temperature, which can be described by the equation $\kappa = \lambda \cdot C_p \cdot d$, where C_p is the specific heat capacity, λ is the thermal diffusivity and d is the density. Near 410 K, the thermal conductivity fluctuations of the KCl flux-grown samples diminish, further supporting the presence of a dual-phase structure. The κ of the material comprises two constituent elements: the carrier thermal conductivity (κ_e) and the lattice thermal conductivity (κ_L), expressed as

$$\kappa = \kappa_e + \kappa_L. \tag{2}$$

The κ_e is linked to σ and the absolute temperature (T) by the Wiedemann–Franz law

$$\kappa_e = L\sigma T. \tag{3}$$

Considering that the Lorenz number (L) in semiconductors is temperature dependent, L was explicitly calculated in this study. The derivation process and related expressions are provided in Section I of the supporting information. The temperature dependence of L is illustrated in Fig. S1, which was subsequently used to separate the contributions of κ_e and κ_L to the total thermal conductivity. The κ_e and κ_L of the material are calculated based on Eqs. (2) and (3), as shown in Figs. 5(e) and 5(f). Within the κ values, the electronic contribution predominates, whereas the KCl flux-synthesized samples exhibit a markedly lower κ_L. This phenomenon can be attributed to two primary factors. Firstly, as evidenced by the cross-sectional SEM image in Fig. 3, the Cu_2Se materials synthesized via the KCl flux method exhibit thinner layered nanostructures than those fabricated by direct melting. These additional interfaces act as scattering centers, leading to more effective scattering of the heat-carrying phonons. Secondly, this study achieved heterovalent doping of Cl^- and K^+ ions into the Cu_2Se lattice, where the significant mismatch in atomic radius between the dopant and host atoms substantially increased the configurational entropy of the system.[46] The enhanced entropy perturbs the atomic arrangement within the crystal lattice, disrupts the long-range order and promotes more effective phonon scattering. This entropy-driven increase in lattice disorder, combined with the higher density of interfaces introduced by the layered nanostructures, effectively reduces the phonon mean free path. As a consequence the flux-assisted Cu_2Se samples exhibit substantially suppressed κ_L, which contributes to the enhancement of their thermoelectric transport properties.[47] The ZT values of each sample at various temperatures were calculated using the measured S, σ and κ, as presented in Fig. 5(d). It is evident that the S_2 sample demonstrates superior ZT values across the entire temperature range owing to its higher S and σ. A peak value of 1.45 is observed at 700 K, indicating its optimal performance at this temperature. The weighted average ZT value over the tested temperature range is 1.03, validating the efficacy and consistency of sample S_2 in generating heat.

Figure 6(a) presents the correlation between carrier concentration (n) and Hall mobility (μ_H) for various Cu_2Se-based materials. Sample S_2 (labeled as 'This work') demonstrates an optimized carrier concentration of approximately 10^{20} cm^{-3} and a moderate Hall mobility of $\sim 45\ cm^2{\cdot}V^{-1}{\cdot}s^{-1}$, falling within the ideal range for achieving a high power factor. As shown in Fig. S3 of the supporting information, the power factor of sample S_2 remains stable at around $1.7 \times 10^{-3}\ W{\cdot}m^{-1}{\cdot}K^{-2}$ in the high-temperature region. Figure 6(b) systematically compares the maximum ZT (ZT_{max}) and the weighted average ZT (ZT_{ave}) values of Cu_2Se-based materials reported in the literature with those of the samples synthesized in this study. It is evident that sample S_2, synthesized via the KCl flux-assisted method, exhibits superior thermoelectric transport performance, ranking among the top levels of currently reported Cu_2Se-based materials. Additional detailed thermoelectric parameters are summarized in Table S1 of Section IV in the supporting information. These results clearly demonstrate that the KCl flux-assisted growth strategy, combined with the co-doping of Cl^- and K^+ ions, effectively regulates the microstructure and carrier transport properties of Cu_2Se. This approach significantly reduces the lattice thermal conductivity while maintaining favorable electrical transport properties, thereby contributing to the overall enhancement of

the thermoelectric performance of Cu_2Se-based materials.

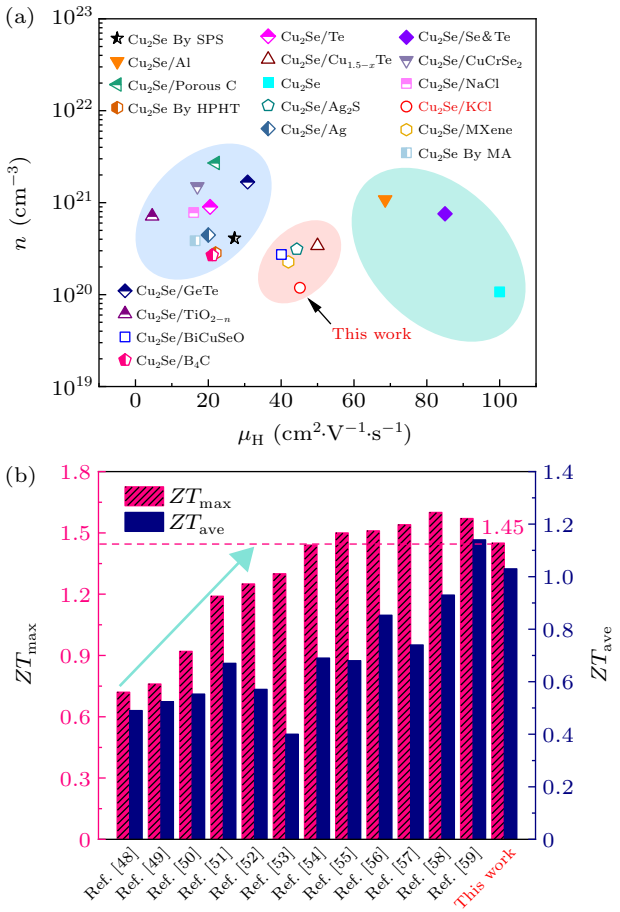


Fig. 6. Comparison of carrier transport properties and thermoelectric performance of Cu_2Se-based materials:[2,5,12,20,48–61] (a) the carrier concentration (n) and Hall mobility (μ_H), (b) ZT_{max} and ZT_{ave}.

4. Conclusion

In conclusion, in this research we successfully fabricated Cu_2Se thermoelectric materials featuring a nanolayered architecture and dual-phase coexistence near 300 K, employing the KCl flux method in conjunction with a high-temperature melting and gradual cooling technique. Comprehensive analyses of the thermoelectric transport properties of all synthesized materials were systematically performed. XRD analysis demonstrates that the samples synthesized employing the KCl flux method exhibit a coexistence of two phases at ambient temperature. This contributes to the enhancement of their overall thermoelectric transport properties. XPS analysis reveals that Cl^- ions, possessing stronger binding energy, substitute for Se^{2-} ions in the lattice, effectively suppressing Cu^+ ion migration and thereby enhancing the structural stability of the material. SEM and TEM analyses demonstrate that all samples synthesized using the KCl flux method exhibit a nanolayered stacking structure and a high density of dislocations, both of which play a crucial role in enhancing phonon scattering and effectively lowering thermal conductivity. Hall effect measurements confirm the effective optimization of carrier mobility in the materials, providing critical insight into how to improve thermoelectric transport properties. In particular, sample S_2 exhibits excellent electrical conductivity over the 300–700 K temperature range, achieving approximately 1.0×10^5 S·m^{-1} at 300 K. The high density of edge dislocations and the incorporation of dopants in the samples prepared via the KCl flux method contribute to an increase in material entropy, which in turn further diminishes the lattice thermal conductivity. At 350 K, the total thermal conductivity of sample S_3 reached an ultra-low value of 0.55 W·m^{-1}·K^{-1}, slightly higher than the lowest value reported in the literature,[2] while the ZT value of sample S_2 reached an impressive 1.45 at 700 K. This study offers novel insights into the regulation of the structure and thermoelectric performance of Cu_2Se using the KCl flux method, demonstrating significant advantages in enhancing electrical conductivity while effectively reducing thermal conductivity.

Acknowledgments

Project supported by the National Natural Science Foundation of China (Grant No. 62464013). The authors would like to express their sincere gratitude to Professor Shukang Deng for his valuable guidance and insightful suggestions throughout this study. The authors also acknowledge Jianjun Wang for his assistance with data processing and analysis.

References

[1] He J and Tritt T M 2017 *Science* **357** eaak9997
[2] Choo S, Lee J, Şişik B, Jung S J, Kim K, Yang S E, Jo S, Nam C, Ahn S, Lee H S, Chae H G, Kim S K, LeBlanc S and Son J S 2024 *Nature Energy* **9** 1105
[3] Fan G, Liu K, Su H, Luo Y, Geng Y, Chen L, Wang B, Mao Z, Sui X and Feng X 2022 *Chemical Engineering Journal* **434** 134702
[4] Byeon D, Sobota R, Delime-Codrin K, Choi S, Hirata K, Adachi M, Kiyama M, Matsuura T, Yamamoto Y, Matsunami M and Takeuchi T 2019 *Nat. Commun.* **10** 72
[5] Yang D, Zhang D, Ao D, Nisar M, Mansoor A, Chen Y, Li F, Ma H, Liang G, Zhang X, Fan P and Zheng Z 2023 *Nano Energy* **117** 108930
[6] Hwang T Y, Choi Y, Song Y, Eom N S A, Kim S, Cho H B, Myung N V and Choa Y H 2018 *Journal of Materials Chemistry C* **6** 972
[7] Zhao L, Islam S M K N, Wang J, Cortie D L, Wang X, Cheng Z, Wang J, Ye N, Dou S, Shi X, Chen L, Snyder G J and Wang X 2017 *Nano Energy* **41** 164
[8] Liu H, Yuan X, Lu P, Shi X, Xu F, He Y, Tang Y, Bai S, Zhang W, Chen L, Lin Y, Shi L, Lin H, Gao X, Zhang X, Chi H and Uher C 2013 *Advanced Materials* **25** 6607
[9] Yang L, Chen Z G, Han G, Hong M and Zou J 2016 *Acta Materialia* **113** 140
[10] Rapaka S S, Anwar S, Singh J and Anwar S 2023 *Physica B* **665** 415044
[11] Zhao K, Liu K, Yue Z, Wang Y, Song Q, Li J, Guan M, Xu Q, Qiu P, Zhu H, Chen L and Shi X 2019 *Advanced Materials* **31** 1903480
[12] Zhao X, Li M, Ma R, Zhang Y and Song H Z 2024 *J. Alloys Compd.* **971** 172787
[13] Tang W, Qian W, Jia S, Li K, Zhou Z, Lan J, Lin Y H and Yang X 2023 *Materials Today Physics* **35** 101104
[14] Yin H, Wang Z Y, Yan X, Zhang Y X, Yang X, Wang C Y, Ge Z and Feng J 2024 *Inorganic Chemistry* **63** 22737
[15] Wang X, Xu Y, Liu X, Tan L, Gu H, Du X and Li D 2024 *Journal of Energy Chemistry* **95** 336

[16] Hu X, Wu Y, Zou Y and Yang G 2024 *Ceramics International* **50** 10285
[17] Yan X, Cao Y, Wang X, Zhang J, Xu S, Li G and Chen B 2024 *Journal of Materials Chemistry C* **12** 13875
[18] Mikami M, Yoshimura M, Mori Y, Sasaki T, Funahashi R and Matsubara I 2002 *Jpn. J. Appl. Phys.* **41** L777
[19] Liu W, Shen L, Shai X, Sun L, Lu J, Chen J, Ge W and Deng S 2019 *CrystEngComm* **21** 6850
[20] Zhao X, Yu T, Zhou B, Ning S, Chen X, Qi N and Chen Z 2024 *ACS Applied Materials & Interfaces* **16** 1333
[21] Nedelcu G, Protesescu L, Yakunin S, Bodnarchuk M I, Grotevent M J and Kovalenko M V 2015 *Nano Lett.* **15** 5635
[22] Zuo X, Chang K, Zhao J, Xie Z, Tang H, Li B and Chang Z 2016 *Journal of Materials Chemistry A* **4** 51
[23] Chen M, Liu W, Ding P, Guo F, Li Z, Chen Y, Yi W, Sun Y, Lu J, Kantorovich L and Yu M 2025 *Nat. Commun.* **16** 1614
[24] Jin H, Wiendlocha B and Heremans J P 2015 *Energy & Environmental Science* **8** 2027
[25] Manthiram A 2022 *ACS Energy Letters* **7** 2404
[26] Yang Y, Wu Q, Deng J, Wang J, Xia Y, Fu X, Tian Q, Zhang L, Yin L J, Tian Y, Xie S Y, Zhang L and Qin Z 2021 *Chin. Phys. B* **30** 116802
[27] Ma X, Shai X, Ding Y, Zheng J, Wang J, Sun J, Li X, Chen W, Wei T, Ren W, Gao L, Deng S and Zeng C 2023 *Molecules* **28** 2629
[28] Liu Y, Hu Z, Tong X, Graf D and Petrovic C 2023 *Phys. Rev. B* **108** 045135
[29] Day T W, Weldert K S, Zeier W G, Chen B R, Moffitt S L, Weis U, Jochum K P, Panthöfer M, Bedzyk M J, Snyder G J and Tremel W 2015 *Chemistry of Materials* **27** 7018
[30] Anjum F, Bhattacharjee D, Bhattacharya A and Maiti T 2025 *Small* **21** 2412711
[31] Ramaswamy P, Devkota S, Pokharel R, Nalamati S, Stevie F, Jones K, Reynolds L and Iyer S 2021 *Scientific Reports* **11** 8329
[32] Zhang Z L, Wang T, Nisar M, Chen Y X, Li F, Chen S, Liang G X, Fan P and Zheng Z H 2023 *Journal of Advanced Ceramics* **12** 1767
[33] Ogawa S, Tsuda Y, Sakamoto T, Okigawa Y, Masuzawa T, Yoshigoe A, Abukawa T and Yamada T 2022 *Applied Surface Science* **605** 154748
[34] Zhao Q, Zhang J, Xia G, Ma S, Fan S, Ping X, Hao L and Zhang Y 2025 *J. Alloys Compd.* **1010** 178224
[35] Ying P, Jian Q, Gong Y, Song T, Yang Y, Geng Y, Huang J, Sun R, Chen C, Shen T, Li Y, Dou W, Liang C, Liu Y, Xiang D, Feng T, Fei X, Zhang Y, Song K, Zhang Y, Wu H and Tang G 2025 *Nat. Commun.* **16** 3305
[36] Wang Q, Li Z, Xue Y, Gao Z, Wang A, Wang J and Wang S 2024 *Appl. Phys. Lett.* **124** 192104
[37] Zhou L, Li Q, Jin M, Zhang R and Zhang Q 2022 *Thin Solid Films* **741** 139024
[38] Xu L, Xiao Y, Wang S, Cui B, Wu D, Ding X and Zhao L D 2022 *Nat. Commun.* **13** 6449
[39] Li P, Phillips N W, Leake S, Allain M, Hofmann F and Chamard V 2021 *Nat. Commun.* **12** 7059
[40] Bai H, Su X, Yang D, Zhang Q, Tan G, Uher C, Tang X and Wu J 2021 *Advanced Functional Materials* **31** 2100431
[41] Rowe D M 2005 *Thermoelectrics handbook: macro to nano* (Boca Raton: CRC Press)
[42] Li B, Li M, Qi H, Zu X, Qiao L and Xiao H 2023 *Crystals* **13** 1586
[43] Zhao C, Li Z, Fan T, Xiao C and Xie Y 2020 *Research* **2020** 9652749
[44] Brown D R, Day T W, Borup K A, Christensen S, Iversen B B and Snyder G J 2013 *APL Materials* **1** 052107
[45] Huang Z, Jiang R, Li P, Liu X, Chen G, Zhao L, Li L, Zhao P, Meng W, Jia S, Zheng H and Wang J 2024 *Nano Today* **58** 102460
[46] Wang W, Liu S, Wang Y, Jia B, Huang Y, Xie L, Jiang B and He J 2024 *Science Advances* **10** eadp4372
[47] Ghosh S, Raman L, Sridar S and Li W 2024 *Crystals* **14** 432
[48] Chen J, Liu T, Bao D, Zhang B, Han G, Liu C, Tang J, Zhou D, Yang L and Chen Z G 2020 *Nanoscale* **12** 20536
[49] Xue L, Zhang Z, Shen W, Ma H, Zhang Y, Fang C and Jia X 2019 *Journal of Materiomics* **5** 103
[50] Zhu Y B, Zhang B P and Liu Y 2017 *Physical Chemistry Chemical Physics* **19** 27664
[51] Xing C, Zhang Y, Xiao K, Han X, Liu Y, Nan B, Ramon M G, Lim K H, Li J, Arbiol J, Poudel B, Nozariasbmarz A, Li W, Ibáñez M and Cabot A 2023 *ACS Nano* **17** 8442
[52] Mac T K, Ta T T, Nguyen H T, Hoang N V, Pham T L H, Duong V T, Pham A T T, Phan B T, Cho S and Duong A T 2023 *Journal of Solid State Chemistry* **322** 123998
[53] Fan P, Hou W, Li L, Li S, Wang J, Cheng Z and Wang C 2023 *Physica B* **654** 414725
[54] Jin Z, Mao T, Qiu P, Yue Z, Wang L, Zhao K, Ren D, Shi X and Chen L 2021 *Materials Today Physics* **21** 100550
[55] Yin Z, Lu R, Bailey T P, Ma T, Uher C and Poudeu P F P 2024 *Chemical Engineering Journal* **501** 157558
[56] Lu J, Li D, Liu W, Shen L, Chen J, Ge W and Deng S 2020 *Chin. Phys. B* **29** 127403
[57] Jian Q, Gong Y, Chen C, Sun R, Zhao S, Shen T, Zhang Q, Geng Y, Li Y, Dou W, Liang C, Liu Y, Xiang D, Ying P and Tang G 2025 *ACS Applied Materials & Interfaces* **17** 15527
[58] Yu J, Liu X, Hu H, Jiang Y, Zhuang H L, Li H, Su B, Li J W, Han Z, Wang Z, Chen L, Hayashi K, Miyazaki Y, Mehdi B L and Li J F 2024 *Joule* **8** 2652
[59] Zhou Z, Huang Y, Wei B, Yang Y, Yu D, Zheng Y, He D, Zhang W, Zou M, Lan J L, He J, Nan C W and Lin Y H 2023 *Nat. Commun.* **14** 2410
[60] Yu J, Hu H, Jiang Y, Zhuang H L, Thong H C, Su B, Li J W, Han Z, Li H, Pei J and Li J F 2024 *Advanced Energy Materials* **14** 2303942
[61] Lourdhusamy V, Paulraj I, Kannan V P and Liu C J 2025 *Journal of Materials Chemistry A* **13** 6027